Mon. Not. R. Astron. Soc. **000**, 1–15 (2001) Printed 8 June 2001 (MN LaTeX style file v1.4)

Universal gas density and temperature profile

E. Komatsu[1,2]⋆ and U. Seljak[3]†
[1]*Department of Astrophysical Sciences, Princeton University, Princeton, NJ 08544, USA*
[2]*Astronomical Institute, Tôhoku University, Aoba, Sendai 980-8578, Japan*
[3]*Department of Physics, Princeton University, Princeton, NJ 08544, USA*

8 June 2001

ABSTRACT
We present an analytic approach to predict gas density and temperature profiles in dark matter haloes. We assume that the gas density profile traces the dark matter profile in outer parts of the haloes, as suggested by a number of hydrodynamic simulations. Under this assumption the hydrostatic equilibrium uniquely fixes the two free parameters in the model, the mass–temperature normalization and the polytropic index, that determine the temperature profile. This enables us to predict a universal gas profile from any universal dark matter profile. Our results show that gas tracing dark matter in the outer parts of the cluster is inconsistent with gas being isothermal and requires temperature to slowly decrease there, in agreement with observations. We compare our predictions for X-ray surface brightness profiles of the haloes and the mass–temperature relation with observations and find that they are generally in a good agreement. We compare the universal profile to the β profile and find that, although the β profile gives a reasonable fit to our predicted profiles, the deviations from it can explain many of the observed trends once the observational selection effects are taken into account. Our model predicts that the mass–temperature relation does not follow the self-similar relation because of the mass dependent halo concentration. We also predict surface brightness profiles of the Sunyaev–Zel'dovich (SZ) effect and find that fitted to the β-profile the core radii and β inferred from the SZ effect are systematically larger than those from the X-ray measurements.

Key words: cosmology: theory – dark matter – galaxies: haloes – galaxies: clusters: general – X-rays: galaxies.

1 INTRODUCTION

The structure of the dark matter haloes has been recognized as one of the most powerful probes of small scale physics, which may potentially distinguish among the competing theoretical models. In cold dark matter (CDM) models, the structure forms through a sequence of mergers, which gives rise to a characteristic density profile of the resulting haloes. Numerical simulations led the way in our understanding of the structure of the haloes. While there is significant scatter among the individual simulated haloes, one finds some similarity among them, justifying the introduction of a universal dark matter halo profile. The density of such a profile changes steeply in the outer parts of haloes, scaling roughly as $\rho \propto r^{-\alpha}$ with $\alpha \sim 3$. The slope gradually becomes shallower in the inner parts, converging to a value between $1 < \alpha < 3/2$ (Navarro, Frenk & White 1996, 1997; Moore et al. 1998). The transition between the two regimes is in general mass dependent, which can be qualitatively explained by the fact that the lower mass haloes collapse at a higher redshift, when the mean density of the universe was higher. This in turn requires a higher central density of the lower mass haloes. Different models make different predictions for the value of the central density as a function of the halo mass as well as for the slope of the inner profile: both CDM and warm dark matter (WDM) predict cuspy haloes, but CDM in general predicts denser haloes at a given mass and radius. Collisional dark matter on the other hand predicts a central core.

While the dark matter density profiles are important, they cannot be easily observed. In this paper, we focus instead on the gas density and temperature profiles, which can be observed through the X-ray emission and the Sunyaev–Zel'dovich (SZ) effect. We introduce a concept of a universal gas density profile in analogy with which universal dark matter profile describes, in an average sense, how the gas density depends on radii. Such a construct is as useful as the universal dark matter density profile, in the sense that

⋆ E-mail: komatsu@astro.princeton.edu
† E-mail: uros@feynman.princeton.edu

it can parameterize, in a simple way, how different cosmological models differ in their predictions for the gas density profile and how can these be used to place constraints on the models from the observations.

By far the most common form used for the gas density profile is the so-called β profile that consists of a central core and a power law outer slope β. While such a profile is useful in observational description of the X-ray clusters, it becomes insufficient when bolometric SZ observations become available. These will measure the gas density profile out to the outer parts of the clusters, where the predicted slope of the profile changes and can no longer be described by a single power law. As we discuss in this paper, there is already some indication that the β profile is insufficient to fully describe the X-ray data. For example, a correlation between core radii and β, found in observational data, can be explained as a consequence of forcing the β profile to describe the underlying gas density profile in which the slope continuously increases with radius. Another shortcoming of the β profile is that it is not derived from a dark matter density profile and thus does not allow one to relate to it in simple terms. Instead, we give a prescription of how to compute the gas density and temperature profiles from any given dark matter density profile, and show that this prescription is unique under our assumptions. The latter property causes our model to differ from similar recent constructions by Makino, Sasaki & Suto (1998) and Suto, Sasaki & Makino (1998).

In order to construct the gas density and temperature profiles, we assume that the gas is in hydrostatic equilibrium throughout the halo. This in itself does not suffice to construct a gas density profile, because the dependence of the temperature on radii remains unspecified. Assuming isothermal profile gives a poor fit to the observed clusters (Makino et al. 1998) and is not favored observationally (Finoguenov, Reiprich & Böhringer 2001). Instead, we make an alternative assumption that the gas density profile traces the dark matter density profile in the outer parts of the halo. While this assumption is qualitatively reasonable, its quantitative justification comes from hydrodynamic simulations that show remarkable agreement between the two profiles in the outer parts of haloes. It is possible that some physics is missing in the current generation of numerical simulations, which for the most part ignore radiative processes. Gas cooling and star formation can affect not only the central regions, but also the global properties of the cluster. However, even in that case, the gas profile in the outer regions remains relatively unaffected (Pearce et al. 2000; Lewis et al. 2000). The remarkable property is that, once this assumption is made, one can derive both the mass–temperature normalization and the temperature dependence on radii analytically, assuming a simple polytropic equation of state. Both are found to be in good agreement with observations as well as simulations. Our assumption that gas temperature has to be monotonic with density limits us to regions outside the central core (roughly outside inner $100-200$ kpc), because in the inner regions gas temperature is often found to be increasing with radius up to $100-200$ kpc and then mildly decreasing again in the outer regions. However, for the most part we will compare our results to observational data for which the central part of the cluster has been excised (e.g. Finoguenov et al. 2001) and we are thus justified to make this assumption. Consequently, our model does not provide constraints on the gas and dark matter profiles in the inner parts of the cluster.

Although the cosmology does not play a major role, for the purpose of this paper we fix the cosmological parameters at the best-fitting values from CMB and large scale structure (Netterfield et al. 2000): $\Omega_{\rm m}=0.3$, $\Omega_\Lambda=0.7$, $\Omega_{\rm b}=0.05$, $h=0.67$, $n=1$, and $\sigma_8=0.9$. All predictions are evaluated at the present epoch ($z=0$).

The structure of this paper is as follows. In §2 we describe the universal dark matter haloes and relations between the virial and observed masses. In §3 we introduce a family of self-similar gas density and temperature profiles, and show how the assumptions fix free parameters in the model. After discussing relations between the virial and observed gas temperatures, the gas density and temperature profiles in haloes are explicitly predicted. In §4 we compare the X-ray surface brightness profiles derived from the predicted gas profiles with the β profile. We study the observational selection effect on the comparison in detail. In §5 we discuss the surface brightness profiles of the SZ effect. In §6 we investigate the mass–temperature relation and compare it to observations. Finally, we summarize our results in §7.

2 UNIVERSAL DARK MATTER DENSITY PROFILES

2.1 Basic properties

A number of high-resolution N-body simulations suggest that the dark matter density profile, $\rho_{\rm dm}(r)$, is well described by a self-similar form. The profile is expressed in terms of a characteristic radius $r_{\rm s}$:

$$\rho_{\rm dm}(r)=\rho_{\rm s}y_{\rm dm}(r/r_{\rm s}), \tag{1}$$

where $\rho_{\rm s}$ is a normalization factor in units of mass density, while $y_{\rm dm}(x)$ is a non-dimensional function representing the profile. $\rho_{\rm s}$ is chosen to represent a characteristic density at a characteristic radius $r=r_{\rm s}$. The characteristic radius describes a typical scale at which the profile slope changes from the outer value to the inner value. Often it is close to the value where the slope is $\alpha=2$ (Navarro et al. 1996, 1997; Moore et al. 1998). Since the dark matter density profile is self-similar, the dark matter mass profile is also self-similar. A dark matter mass enclosed within a radius r is

$$M(\leq r)\equiv 4\pi\rho_{\rm s}r_{\rm s}^3 m\left(r/r_{\rm s}\right), \tag{2}$$

where $m(x)$ is a non-dimensional mass profile given by

$$m(x)\equiv\int_0^x du\ u^2 y_{\rm dm}(u). \tag{3}$$

$y_{\rm dm}(u)$ must be shallower than u^{-3} in the central region in order for the mass to converge.

We define a total dark matter mass, $M_{\rm vir}$, as a mass within the virial radius, $r_{\rm vir}$, i.e., $M_{\rm vir}\equiv M(\leq c)$, where

$$c\equiv\frac{r_{\rm vir}}{r_{\rm s}} \tag{4}$$

is a dimensionless parameter called the concentration parameter. Evaluating equation (2) at the virial radius, we fix the normalization factor $\rho_{\rm s}$ as

$$\rho_{\rm s} = c^3 \frac{M_{\rm vir}}{4\pi r_{\rm vir}^3 m(c)}. \tag{5}$$

The virial radius, $r_{\rm vir}(M_{\rm vir}, z)$, is calculated by the spherical collapse model (Peebles 1980),

$$r_{\rm vir} = \left[\frac{M_{\rm vir}}{(4\pi/3)\Delta_{\rm c}(z)\rho_{\rm c}(z)}\right]^{1/3}, \tag{6}$$

where $\Delta_{\rm c}(z)$ is a spherical over-density of the virialized halo within $r_{\rm vir}$ at z in units of the critical density of the universe at z, $\rho_{\rm c}(z)$. In the Einstein–de Sitter universe model, $\Delta_{\rm c}(z)$ is independent of z, and is exactly $18\pi^2 \simeq 178$. Lacey & Cole (1993) and Nakamura & Suto (1997) provide $\Delta_{\rm c}(z)$ for arbitrary cosmological models. In our cosmological model with $\Omega_{\rm m} = 0.3$ and $\Omega_\Lambda = 0.7$, $\Delta_{\rm c}(z=0) = 100$. Thus, the only parameter in this framework is the concentration parameter, c, which can be used instead of $\rho_{\rm s}$. A number of N-body simulations suggest that c gradually decreases with the virial mass. Assuming that the dependence of c is known, for example, from N-body simulations (Bullock et al. 2001; Eke, Navarro & Steinmetz 2000), or from the non-linear dark matter power spectrum (Seljak 2000), one can predict $\rho_{\rm dm}(r)$ for any $M_{\rm vir}$, any z, and in principle any cosmological models. This is the main advantage of the universal dark matter density profile paradigm that explains its popularity in recent work. Although the universal profile does not explain the dark matter profiles on an object to object basis (Jing & Suto 2000; Klypin et al. 2001), it is still successful in fitting the averaged form of the dark matter density profiles with reasonable accuracy.

So far we have only discussed the functional dependence of the profile on the characteristic radius. For a complete description to be made, we also need to have the functional form of $y_{\rm dm}(x)$. We adopt the following form:

$$y_{\rm dm}(x) = \frac{1}{x^\alpha(1+x)^{3-\alpha}}. \tag{7}$$

The asymptotic profile in $x \gg 1$ regime is $y_{\rm dm}(x \gg 1) = x^{-3}$. This is the most common value found in the N-body simulations, although scatter around this value can be quite significant (Thomas et al. 2001). In the inner parts of haloes, we have $y_{\rm dm}(x \ll 1) = x^{-\alpha}$. Particularly, $\alpha = 1$ corresponds to the profile proposed by Navarro et al. (1996, 1997), while $\alpha = 3/2$ corresponds to the one proposed by Moore et al. (1998) and Jing & Suto (2000). We will focus on these two particular cases throughout this paper. Using these parameters, Suto et al. (1998) evaluated the relevant integrals for $\alpha = 1$:

$$m(x) = \ln(1+x) - \frac{x}{1+x}, \tag{8}$$

$$\int_0^x du \frac{m(u)}{u^2} = 1 - \frac{\ln(1+x)}{x}, \tag{9}$$

and for $\alpha = 3/2$:

$$m(x) = 2\ln\left(\sqrt{x} + \sqrt{1+x}\right) - 2\sqrt{\frac{x}{1+x}}, \tag{10}$$

$$\int_0^x du \frac{m(u)}{u^2} = -\frac{2\ln\left(\sqrt{x}+\sqrt{1+x}\right)}{x} + 2\sqrt{\frac{1+x}{x}}. \tag{11}$$

$\int_0^x du u^{-2} m(u)$ will be used in next section.

There are several different empirical fitting formulae for the concentration parameter in the literature. A recent compilation is found in Eke et al. (2000). For $\alpha = 1$, we will use the one used in Seljak (2000):

$$c = 6\left(\frac{M{\rm vir}}{10^{14}h^{-1}M_\odot}\right)^{-1/5}. \tag{12}$$

For $\alpha = 3/2$ one must reduce the concentration parameter roughly by a factor of 1.7 (Seljak 2000; Klypin et al. 2001).

2.2 Overdensity radius and mass

In many cases, X-ray observations are not sufficiently sensitive to measure X-ray surface brightness and gas temperature profiles out to the virial radius. Therefore, instead of measuring the virial mass, many authors measure the mass enclosed within an overdensity radius, r_δ, at which the dark matter density is δ times the critical density of the universe:

$$r_\delta \equiv \left[\frac{M(\le r_\delta)}{(4\pi/3)\delta\rho_{\rm c}(z)}\right]^{1/3}. \tag{13}$$

Note that the virial radius at $z = 0$ corresponds to r_{100} in our cosmological model, as $\Delta_{\rm c}(0) = 100$ in equation (6). Since we assume the dark matter density profile, and hence the mass profile, is known, we can relate $M_{\rm vir}$ to $M(\le r_\delta)$ by solving the equation

$$M(\le r_\delta) = \left[\frac{m(r_\delta/r_{\rm s})}{m(c)}\right] M_{\rm vir} = \left[\frac{m(cr_\delta/r_{\rm vir})}{m(c)}\right] M_{\rm vir}. \tag{14}$$

Figure 1 plots $M(\le r_{500})$ as a function of $M_{\rm vir}$ for $\alpha = 1$ and 3/2. The mass dependence arises solely from the mass scaling of the concentration parameter given by equation (12). Since we will primarily be looking at haloes with the mass between $10^{13}h^{-1}M_\odot$ and $10^{15}h^{-1}M_\odot$, the relation between the two is roughly $M(\le r_{500}) \sim M_{\rm vir}/2$. The mass measurement using the gas density profiles out to r_{500} is thought to be accurate (e.g. Evrard, Metzler & Navarro 1996). This is why this radius has been frequently used in the literature. Therefore, we will use r_{500} and $M(\le r_{500})$ for comparison of our theoretical predictions to observations. Figure 1 also plots a ratio of r_{500} to the virial radius as a function of $M_{\rm vir}$, and one finds r_{500} is about one half of the virial radius. Note that there is some ambiguity in the definition of the virial radius. Some authors use a fixed overdensity independent of cosmology, and others use the spherical collapse value that we use. Although we will continue to use the concentration as defined in equation (4), we may also introduce a more model independent quantity, $c_{500} = r_{500}/r_{\rm s}$, which does not depend on the definition of the virial radius. For the cosmology used here it is given by $c_{500} \sim c/2$.

3 SELF-SIMILAR GAS DENSITY AND TEMPERATURE PROFILES

3.1 Polytropic gas model in hydrostatic equilibrium

Since the dark matter density profile is assumed to be self-similar, a gas density profile, $\rho_{\rm gas}(r)$, would also be self-similar, as long as no additional scale is introduced (this

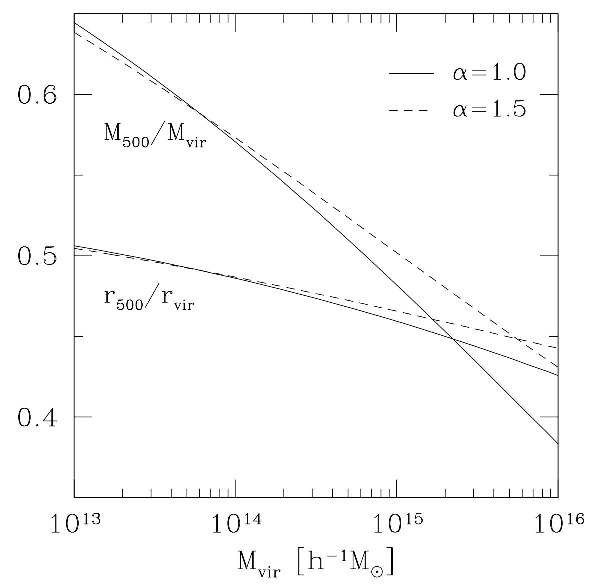

Figure 1. Ratio of the virial mass, $M_{\rm vir}$, to the overdensity mass at r_{500}, $M_{500} \equiv M(\le r_{500})$, as a function of $M_{\rm vir}$. Ratio of r_{500} to the virial radius, $r_{\rm vir}$, is also shown. The solid lines represent $\alpha = 1$, while the dashed lines represent $\alpha = 3/2$.

translates into a requirement that the density-temperature relation is a power law). Thus, we have

$$\rho_{\rm gas}(r) = \rho_{\rm gas}(0) y_{\rm gas}(r/r_{\rm s}), \tag{15}$$

where $\rho_{\rm gas}(0)$ denotes the gas density at $r = 0$. We can parameterize it in this way because, in contrast to the dark matter density profile, a flat gas density core near the centre of haloes is well observed at least for fairly massive clusters and is expected if the gas temperature is not a strong function of radii. Makino et al. (1998) and Suto et al. (1998) showed that the hydrostatic equilibrium between the gas pressure and the self-similar dark matter potential gives the self-similar form of the gas density profile.

In order to phenomenologically take into account the effect of the gas temperature gradient that is found both in observations and hydrodynamic simulations, Suto et al. (1998) parametrized the gas pressure in a polytropic form, $P_{\rm gas} \propto \rho_{\rm gas} T_{\rm gas} \propto \rho_{\rm gas}^{\gamma}$, which implies the self-similar temperature profile:

$$T_{\rm gas}(r/r_{\rm s}) = T_{\rm gas}(0) y_{\rm gas}^{\gamma-1}(r/r_{\rm s}). \tag{16}$$

Then, the hydrostatic equilibrium equation,

$$\rho_{\rm gas}^{-1} \frac{dP_{\rm gas}}{dr} = -G \frac{M(\le r)}{r^2}, \tag{17}$$

gives

$$\frac{dy_{\rm gas}^{\gamma-1}(r/r_{\rm s})}{dr} = -\left(\frac{\gamma-1}{\gamma}\right) \frac{G\mu m_{\rm p} M_{\rm vir}}{k_{\rm B} T_{\rm gas}(0) r^2} \left[\frac{m(r/r_{\rm s})}{m(c)}\right]. \tag{18}$$

$M_{\rm vir}$ is the virial mass, and $m(x)$ is the dimensionless mass profile given by equation (3). Since we defined $y_{\rm gas}(r)$ so as $y_{\rm gas}(0) = 1$ (see equation (15)), equation (18) is formally solved for $y_{\rm gas}(x)$ as (Suto et al. 1998)

$$y_{\rm gas}^{\gamma-1}(x) = 1 - 3\eta^{-1}(0)\left(\frac{\gamma-1}{\gamma}\right)\left[\frac{c}{m(c)}\right]\int_0^x du \frac{m(u)}{u^2}, \tag{19}$$

where

$$\eta^{-1}(x) \equiv \frac{G\mu m_{\rm p} M_{\rm vir}}{3 r_{\rm vir} k_{\rm B} T_{\rm gas}(x)} \tag{20}$$

is the normalization factor relating $T_{\rm gas}(x)$ to $M_{\rm vir}$. The hydrostatic equation (18) does not include $\rho_{\rm gas}(0)$, but $\eta(0)$ representing $T_{\rm gas}(0)$; thus, $\eta(0)$ is one of two free parameters in this model. The other parameter is the polytropic index γ. As we shall see below, both will be fixed by the requirement that the gas and the dark matter profiles agree outside the cluster core.

3.2 Gas tracing dark matter outside the core

The main ingredient of our model is to assume that the gas density profile traces the dark matter density profile in the outer region of the halo. Qualitatively this assumption is reasonable, as the gas and the dark matter obey similar equations of motion to each other. The main difference is that the gas infalling into the cluster potential-well is shocked and then heated, while the dark matter, being collisionless, does not undergo shock heating. What it does undergo is orbit mixing that causes multiple streams to appear at the same physical position. This gives rise to the velocity dispersion that can be viewed as an effective temperature of the dark matter. Taking moments of the collisionless Boltzmann equation leads to the Jeans equations (Binney & Tremaine 1987) that are formally similar to the gas fluid equations. The main difference is that for the case of the collisionless system the effective pressure is the velocity dispersion tensor that can be anisotropic, unlike in the case of gas.

A better reason for this assumption is that this is observed in a number of hydrodynamic simulations (Navarro, Frenk & White 1995; Bryan & Norman 1998; Eke, Navarro & Frenk 1998; Frenk et al. 1999; Pearce et al. 2000; Lewis et al. 2000; Yoshikawa, Jing & Suto 2000). These simulations suggest that the gas density profile traces the dark matter density profile for $r \gtrsim r_{\rm vir}/2$. For example, in the Santa Barbara cluster project (Frenk et al. 1999), a comparison of a dozen numerical codes for a single cluster, all of which show this property for this one particular cluster. The agreement is quite remarkable and accurate to 10% or better. Other larger samples also show the similar agreement. While additional physics missing in the non-radiative simulations, such as cooling and star formation, can change the structure of the gas, the outer regions appear to remain relatively unaffected (Pearce et al. 2000; Lewis et al. 2000).

We use this assumption in our model by requiring the gas density profile, $y_{\rm gas}(x)$, to match the dark matter density profile, $y_{\rm dm}(x)$, at a certain matching point x_*. We impose this by requiring slopes of these two profiles to be the same,

$$s_* \equiv \left.\frac{d\ln y_{\rm dm}(x)}{\ln x}\right|_{x=x_*} = \left.\frac{d\ln y_{\rm gas}(x)}{\ln x}\right|_{x=x_*}, \tag{21}$$

where s_* denotes an effective slope of the dark matter density profile at x_*. Substituting the explicit form of $y_{\rm dm}(x)$ (equation (7)) into equation (21), we obtain the effective slope that the gas density profile has at x_*:

$$s_* = -\left[\alpha + (3-\alpha)\frac{x_*}{1+x_*}\right]. \quad (22)$$

This constraint fixes one of the two parameters of the model, $\eta(0)$, that is the normalization factor for the mass–temperature relation given by equation (20). Substituting the solution for $y_{\rm gas}(x)$ from equation (19) and the effective slope from equation (22) into equation (21), we obtain the solution for $\eta(0)$ as

$$\eta(0) = \gamma^{-1}\left\{\left(\frac{-3}{s_*}\right)\left[\frac{x_*^{-1}m(x_*)}{c^{-1}m(c)}\right] + 3(\gamma-1)\left[\frac{c}{m(c)}\right]\int_0^{x_*} du\frac{m(u)}{u^2}\right\}. \quad (23)$$

In the isothermal limit, $\gamma \to 1$, we have

$$\eta(0) = \left(\frac{-3}{s_*}\right)\left[\frac{x_*^{-1}m(x_*)}{c^{-1}m(c)}\right]. \quad (24)$$

Note that this gives $\eta(0) = 1$ in the limit of large concentration.

In order for the two profiles to agree over a wide range, the slopes of the two should be similar to each other not only at $x = x_*$, but everywhere in the outer region of haloes, so within a factor of two above and below the virial radius ($c/2 < x < 2c$) according to the simulations. In only this way the solution will not depend on the choice of x_*. This requirement will not be satisfied in general. However, we still have one free parameter left, the polytropic index γ. We fix it by requiring that the solution for $\eta(0)$ does not depend on x_*. In this way our model no longer contains any free parameters left. The gas temperature at an arbitrary radial point is calculated from $\eta(r) = \eta(0)y_{\rm gas}^{\gamma-1}(r)$.

Figure 2 plots $\eta(0)$ as a function of the matching point x_* for a variety of polytropic indices γ. It is clear from this figure that $\gamma = 1.1 - 1.2$ satisfy the requirement that $\eta(0)$ is independent of x_*. The isothermal case with $\gamma = 1$ fails this requirement, meaning that the isothermal gas density profile cannot be made similar to the dark matter density profile in the outer parts of the halo. The best value of γ depends very weakly on c, changing from 1.2 to 1.1 as c varies from 4 to 10 (or the mass from $M_{\rm vir} = 10^{13}M_\odot$ to $10^{15}M_\odot$). A simple linear fit is found to be

$$\gamma = 1.15 + 0.01\,(c_{\rm NFW} - 6.5), \quad (25)$$

where $c_{\rm NFW}$ denotes the concentration parameter for the dark matter density profile with $\alpha = 1$. Equation (25) gives an adequate value to both $\alpha = 1$ and $\alpha = 3/2$ profiles. Here, note that the concentration for $\alpha = 3/2$ is given by $c = c_{\rm NFW}/1.7$. Thus, γ is no longer a free parameter, but is fixed.

Furthermore, combining equation (23) with (25) gives $\eta(0)$ as a function of the concentration parameter. Figure 3 plots $\eta(0)$ as a function of $c_{\rm NFW}$. We find that the dependence of $\eta(0)$ on $c_{\rm NFW}$ is well fitted by

$$\eta(0) = 0.00676\,(c_{\rm NFW} - 6.5)^2 + 0.206\,(c_{\rm NFW} - 6.5) + 2.48, \quad (26)$$

for $\alpha = 1$, and

$$\eta(0) = 0.00776\,(c_{\rm NFW} - 6.5)^2 + 0.264\,(c_{\rm NFW} - 6.5) + 3.07, \quad (27)$$

for $\alpha = 3/2$. Thus, the higher concentration implies the higher central gas temperature than the gas temperature at the virial radius. Since by construction the particular choice of x_* does not affect our analysis, we take $x_* = c$ (or $r_* = r_{\rm vir}$) for definiteness in the following.

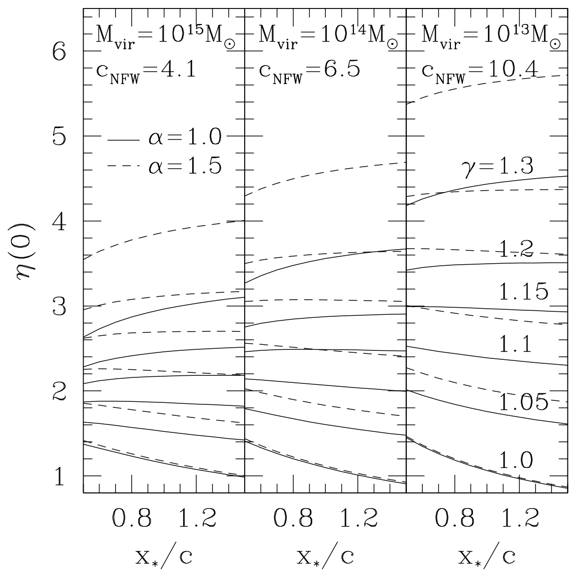

Figure 2. Mass–temperature normalization factor at the centre, $\eta(0)$, predicted by the polytropic gas model with a polytropic index of γ. $\eta(0)$ is plotted as a function of the matching point x_* in units of the concentration parameter c. The solid lines represent $\alpha = 1$, while the dashed lines represent $\alpha = 3/2$. From left to right panels, $M_{\rm vir} = 10^{15}$, 10^{14}, and 10^{13} $M_\odot$ are plotted. Each mass corresponds to the concentration parameter of $c_{\rm NFW} = 4.1$, 6.5, and 10.4 for $\alpha = 1$, respectively, while $c = c_{\rm NFW}/1.7$ for $\alpha = 3/2$. In each panel, the cases of $\gamma = 1.0$, 1.05, 1.1, 1.15, 1.2 and 1.3 are plotted from bottom to top lines.

Figure 4 shows histograms of observationally measured polytropic indices. The top panel plots the whole sample from Finoguenov et al. (2001). There is a peak in the population around $\gamma \simeq 1.1$ with a mean value of $\gamma = 1.15$ that is close to our best value given by equation (25). The bottom panel of this figure plots the hotter objects than 3 keV in the solid line, and the cooler ones below it in the dashed line. The distribution is basically the same for those different temperatures. Thus, there is no significant dependence of the polytropic indices on the gas temperature. This is also in agreement with our model.

3.3 Emission- and mass-weighted mean gas temperatures

Since X-ray observations do not measure the gas temperature itself but the emission-weighted mean temperature, the latter is the quantity that one must use as a representative gas temperature of the halo. If the halo is isothermal, then the gas temperature and the emission-weighted mean temperature are the same. The temperature gradient makes them different. The emission-weighted mean temperature, $T_{\rm X}$, is predicted by this spherical polytropic gas model to be

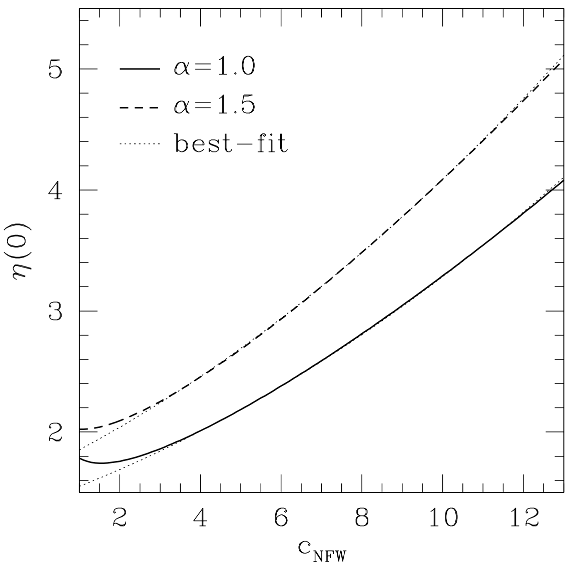

Figure 3. Mass–temperature normalization factor at the centre, $\eta(0)$, as a function of the concentration parameter in the dark matter density profile for $\alpha = 1$, c_{NFW}. The solid line represents $\alpha = 1$, while the dashed line represents $\alpha = 3/2$. The dotted lines are the best-fitting lines given by equations (26) and (27).

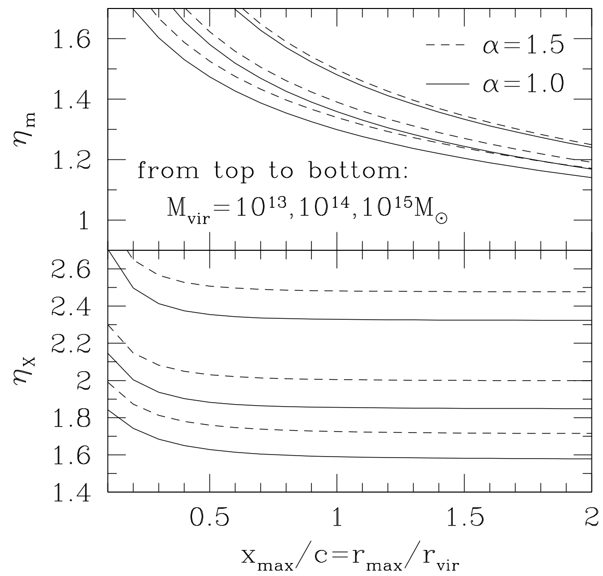

Figure 5. Predicted mass–temperature normalization factors as a function of the upper boundary of the integration, $x_{\max}$, in equations (29) and (30). The bottom panel is the emission-weighted normalization factor, while the top panel is the mass-weighted one. The solid lines use the dark matter density profile for $\alpha = 1$, while the dashed lines use the one for $\alpha = 3/2$. From top to bottom lines, $M = 10^{15}$, 10^{14}, and $10^{13} M_\odot$ are shown.

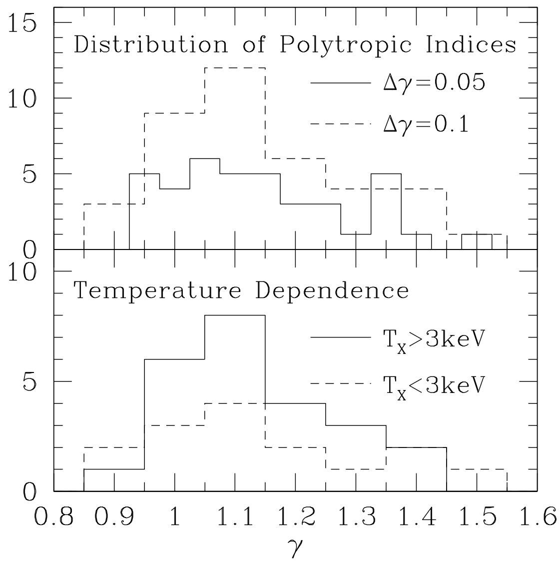

Figure 4. Measured distribution of the polytropic indices, γ, from Finoguenov et al. (2001). The top panel plots the whole sample in two different bins. The solid line is $\Delta\gamma = 0.1$ bin, while the dashed line is $\Delta\gamma = 0.05$ bin. The mean value of γ over the whole sample is 1.15. The bottom panel plots the temperature dependence of γ. The solid line shows the clusters above 3 keV, while the dashed line shows the cooler ones below 3 keV. There is no clear evidence that the polytropic index changes with temperature.

(Suto et al. 1998)

$$T_{\mathrm{X}} \equiv \frac{\int dV \rho_{\mathrm{gas}}^2 \Lambda(T_{\mathrm{gas}}) T_{\mathrm{gas}}}{\int dV \rho_{\mathrm{gas}}^2 \Lambda(T_{\mathrm{gas}})}$$
$$\approx T_{\mathrm{gas}}(0) \left[\frac{\int_0^{x_{\max}} x^2 dx \left[y_{\mathrm{gas}}(x)\right]^{(3\gamma+1)/2}}{\int_0^{x_{\max}} x^2 dx \left[y_{\mathrm{gas}}(x)\right]^{(\gamma+3)/2}} \right], \quad (28)$$

where we have approximated the cooling function, $\Lambda(T_{\mathrm{gas}})$, with the bolometric bremsstrahlung, $\Lambda(T_{\mathrm{gas}}) \propto T_{\mathrm{gas}}^{1/2}$. Since we do not attempt to predict the X-ray luminosity but the X-ray temperature, this approximation seems sufficient. For a practical evaluation of T_{X}, we should care how to choose $x_{\max}$. As $y_{\mathrm{gas}}(x) \propto x^{s_*} \approx x^{-3}$ for $x \gg 1$, $x^3 \left[y_{\mathrm{gas}}(x)\right]^{(\gamma+3)/2} \propto x^{-3(\gamma+1)/2}$. Thus, the integration in the denominator of equation (28) converges rapidly as x^{-3}. The numerator converges even more rapidly than the denominator as long as $\gamma > 1$. This rapid convergence implies that a specific choice of $x_{\max}$ has no systematic effect on T_{X}. Therefore, we conclude that T_{X} calculated from our model can be robustly compared to observations as well as simulations. The bottom panel of figure 5 plots the sensitivity of T_{X} to $x_{\max}$. The plotted quantity, η_{X}, is the emission-weighted mass–temperature normalization factor defined by equation (29) below, and is equivalent to T_{X}. As expected, T_{X} is quite insensitive to $x_{\max}$ as long as $x_{\max} \gtrsim 0.2c \sim 0.4 r_{500}/r_{\mathrm{s}}$. Thus, we use $x_{\max} = c$ for definiteness.

For comparison to both observations and simulations, the normalization factor of the mass–temperature relation, $\eta(r)$ (equation (20)), should be replaced by the emission-weighted mean normalization factor

$$\eta_{\rm X} \equiv \frac{\int dV \rho_{\rm gas}^2 \Lambda(T_{\rm gas})\eta(r)}{\int dV \rho_{\rm gas}^2 \Lambda(T_{\rm gas})} \approx \frac{\int_0^{x_{\rm max}} x^2 dx\, [y_{\rm gas}(x)]^{(\gamma+3)/2}\, \eta(x)}{\int_0^{x_{\rm max}} x^2 dx\, [y_{\rm gas}(x)]^{(\gamma+3)/2}}. \quad (29)$$

This normalization factor has been frequently calculated in several hydrodynamic simulations (Evrard et al. 1996; Bryan & Norman 1998; Eke et al. 1998; Yoshikawa et al. 2000; Thomas et al. 2001). For instance, $\eta_{\rm X}$ corresponds to the emission-weighted γ in Yoshikawa et al. (2000), $(3/2)f_{\rm T}$ in Bryan & Norman (1998), and $(3/2)\overline{\beta}_{\rm TM}^{-1}$ in Eke et al. (1998). Since the emission-weighted mean temperature is significantly weighted toward the central region of haloes, it could be sensitive to the numerical resolution (Lewis et al. 2000). We find that there is significant dispersion of $\eta_{\rm X}$ among different hydrodynamic simulations, in contrast to the mass-weighted mean normalization factor defined as (Yoshikawa et al. 2000; Thomas et al. 2001):

$$\eta_{\rm m} \equiv \frac{\int dV \rho_{\rm gas}\eta(r)}{\int dV \rho_{\rm gas}} = \frac{\int_0^{x_{\rm max}} x^2 dx\ y_{\rm gas}(x)\eta(x)}{\int_0^{x_{\rm max}} x^2 dx\ y_{\rm gas}(x)}. \quad (30)$$

This is less weighted towards the central region of haloes than the emission-weighted normalization. While it should be less sensitive to the numerical resolution of simulations, it is not directly observable from the X-ray observations. In contrast to the emission-weighted normalization, the denominator of equation (30) does not converge, but diverges logarithmically. The numerator converges if $\gamma > 1$, but very slowly. The top panel of figure 5 plots the sensitivity of $\eta_{\rm m}$ to $x_{\rm max}$. As expected, $\eta_{\rm m}$ is rather sensitive to $x_{\rm max}$, in contrast to $\eta_{\rm X}$. Thus, in order for $\eta_{\rm m}$ to be compared to simulations, we use the virial radius $x_{\rm max} = c$ used in Thomas et al. (2001).

Applying this to our gas model, we calculate $\eta_{\rm X}$ and $\eta_{\rm m}$ as a function of the halo mass. This is shown in figure 6 for both profiles with $\alpha = 1$ and 3/2. In order to facilitate the comparison with previous work, we plot the dependence against the virial mass, rather than the concentration parameter, but the two are related to each other through equation (12). We find that $\eta_{\rm X} > \eta_{\rm m}$, i.e., $T_{\rm X} > T_{\rm m}$, as observed in hydrodynamic simulations carried out by Yoshikawa et al. (2000) and Thomas et al. (2001). This is because the emission-weighted mean temperature is much more weighted towards the denser central region than the mass-weighted one, where the gas temperature is higher as long as $\gamma > 1$.

We also find that in both cases the values increase as the mass decreases, more so for $\eta_{\rm X}$ than for $\eta_{\rm m}$. This is caused by the concentration dependence of the halo mass. It reflects the fact that the density in the core for higher c (lower mass) is larger than for lower c (higher mass). This in turn gives a higher temperature because of the assumed polytropic relation between the gas density and temperature.

A number of hydrodynamic simulations in the literature give the mass–temperature normalization factors weighted by either the emission or the mass. Figure 6 compares our predictions to those obtained from the simulations. Overall, the predicted normalizations are in reasonable agreement with the simulations in the high mass regime (except for simulations by Bryan & Norman (1998) who predict 20% lower normalizations compared to the other simulations and to our results). Our predicted emission-weighted normalizations are higher than simulated ones for less massive haloes. It is possible that this is caused by a poorer numerical resolution for less massive haloes. It is also possible that the mass dependence has not been noticed, as most of previous work relied on a self-similar model for comparison in which there is no mass dependence of the concentration parameter. The predicted mass-weighted normalizations that are less sensitive to the resolution issues agree better with the simulations. The comparison with observations is presented in the next section.

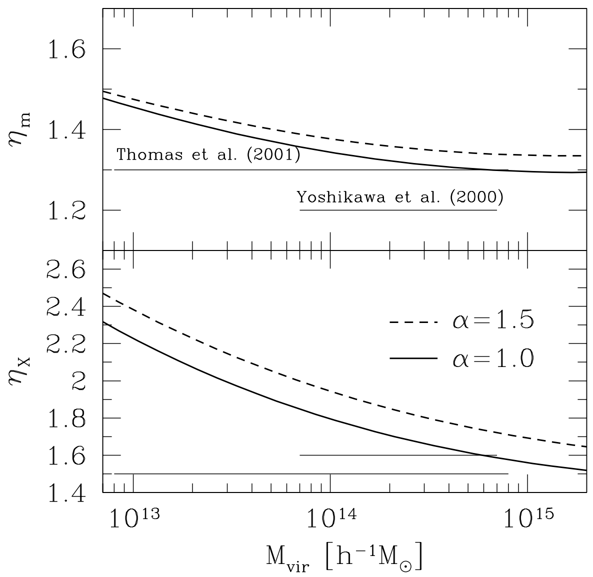

Figure 6. Predicted mass–temperature normalization factors as a function of the virial mass $M_{\rm vir}$. The emission-weighted normalization factor, $\eta_{\rm X}$ (equation (29)), is plotted in the bottom panel, while the mass-weighted one, $\eta_{\rm m}$ (equation (30)), is plotted in the top panel. The thick solid lines represent $\alpha = 1$, while the thick dashed lines represent $\alpha = 3/2$. The thin solid lines indicate the normalization factors derived from hydrodynamic simulations carried out by Thomas et al. (2001) (upper line in the top panel and lower line in the bottom panel) and Yoshikawa et al. (2000) (lower line in the top panel and upper line in the bottom panel).

3.4 Predicted gas density and gas temperature profiles

We plot the dark matter and the gas density profiles in figure 7 for $M = 10^{15}$, 10^{14}, and $10^{13} M_\odot$ from left to right panels. $\alpha = 3/2$ is plotted in the top panels, while $\alpha = 1$ is plotted in the bottom panels. The dark matter density profiles are plotted as the dashed lines, while the gas density profiles are plotted as the solid lines. As assumed the gas and the dark matter density profiles are very similar to each other in the outer parts of the haloes. The gas density profile is always shallower than the dark matter density profile in the central part of the halo, and it develops an approximate core. This is because the large thermal gas pressure in the

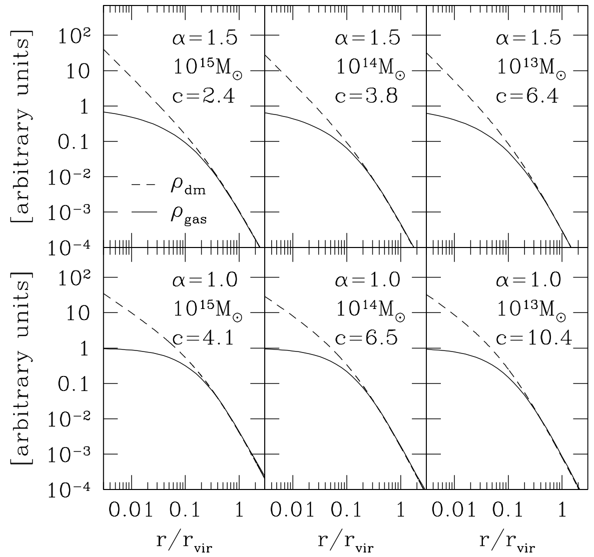

Figure 7. Predicted gas density profiles (solid lines) shown with universal dark matter density profiles (dashed lines). The top panels use the dark matter density profile for $\alpha = 3/2$, while the bottom panels use the one for $\alpha = 1$. From left to right panels, each panel shows the case of $M = 10^{15}$, 10^{14}, and $10^{13} M_\odot$, respectively. The corresponding concentration parameter, c, to the mass is quoted.

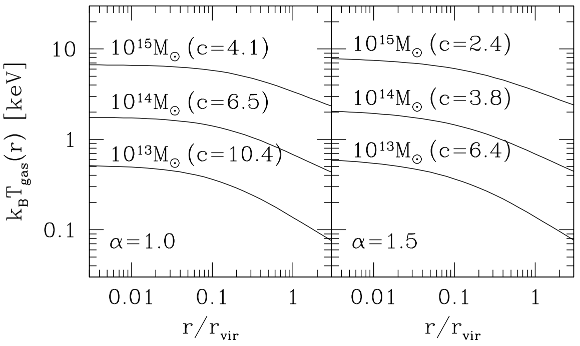

Figure 8. Predicted gas temperature profiles. The left panel uses the dark matter density profile for $\alpha = 1$, while the right panel uses the one for $\alpha = 3/2$. From top to bottom lines, $M = 10^{15}$, 10^{14}, and $10^{13} M_\odot$ are shown. The corresponding concentration parameter, c, to the mass is quoted.

centre balances the force of gravity exerted on the gas fluid element even for a nearly uniform gas density. These profiles are in very good agreement with those found in numerical simulations (Eke et al. 1998; Frenk et al. 1999; Pearce et al. 2000; Lewis et al. 2000; Yoshikawa et al. 2000), where the gas profile is similarly smoother in the centre.

Figure 8 plots the gas temperature profiles for $M = 10^{15}$, 10^{14}, and $10^{13} M_\odot$ from left to right panels, for $\alpha = 3/2$ in the top panels and $\alpha = 1$ in the bottom panels. These profiles are also in reasonable agreement with the profiles observed in the simulations (Navarro et al. 1995; Eke et al. 1998; Bryan & Norman 1998; Frenk et al. 1999; Pearce et al. 2000; Yoshikawa et al. 2000; Thomas et al. 2001).

The predicted gas density profile for $M = 10^{15} M_\odot$ is remarkably similar to the simulated cluster by Frenk et al. (1999) that has $M = 1.1 \times 10^{15} M_\odot$. The predicted temperature is also in good agreement with it and the profile shows a decline in temperature with radius described with $\gamma = 1.1 - 1.2$. Using a larger sample simulated by Thomas et al. (2001), one finds the best value around $\gamma = 1.1$, again in good agreement with our predictions.

The simulations discussed above are all without the radiative processes, and so one may worry that including cooling and star formation may change the results and make the agreement worse. This has been investigated by Lewis et al. (2000), who conclude that the addition of these processes modifies not only the central properties, but also the global structure of the haloes to some extent. Nevertheless, they also find that $\gamma = 1.1 - 1.2$ gives good fit to their simulated results outside the core and inside the virial radius regardless of the inclusion of the cooling effect.

We conclude that our predicted profiles with the polytropic index fixed by equation (25) are in good agreement with both the observations and hydrodynamic simulations, at least outside the core. Recent *Chandra* (McNamara et al. 2000; Allen, Ettori & Fabian 2001; Allen et al. 2001) and *XMM–Newton* (Arnaud et al. 2001a, 2001b; Kaastra et al. 2001) observations indicate that inside the core the gas temperature rises with radii, which cannot be described within our model with $\gamma \sim 1.15$. We will thus not attempt to extend this model and the predicted temperature profile to scales much below the core radius.

4 COMPARISON TO OBSERVED X-RAY SURFACE BRIGHTNESS PROFILES

4.1 Spherical β profile

Historically, X-ray observations have been interpreted using the spherical β profile:

$$I_X(r) = I_X(0)\left[1 + \left(\frac{r}{r_c^X}\right)^2\right]^{1/2-3\beta_X}, \tag{31}$$

where r_c^X is the projected X-ray core radius. This profile had a remarkable success in fitting observed X-ray surface brightness profiles, except for the very central parts of haloes, where the radiative cooling effect seems to play a major role. This region is often excluded by observers when they fit the measured X-ray profile to the β profile above. Therefore, in order to compare our predicted profiles with observationally measured X-ray surface brightness profiles, we fit the core radius and β_X to our predicted X-ray surface brightness profile:

$$I_X(x) \quad \propto \quad \int_{-\infty}^{\infty} dl\ \rho_{gas}^2 \Lambda(T_{gas})$$

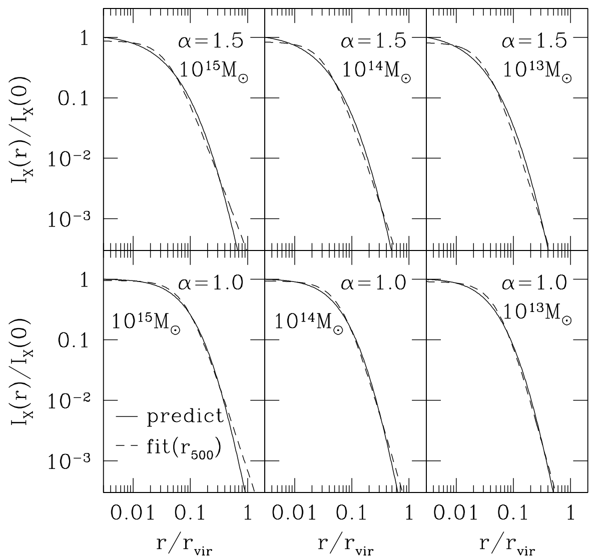

Figure 9. Predicted X-ray surface brightness profiles (solid lines) and the best-fitting spherical β profiles (dashed lines). The fit is performed out to r_{500}. Note that r_{500} is about one half of the virial radius (see figure 1). The top panels use the dark matter density profile for $\alpha = 3/2$, while the bottom panels use the one for $\alpha = 1$. From left to right panels, each panel shows the case of $M = 10^{15}$, 10^{14}, and $10^{13} M_{\odot}$, respectively.

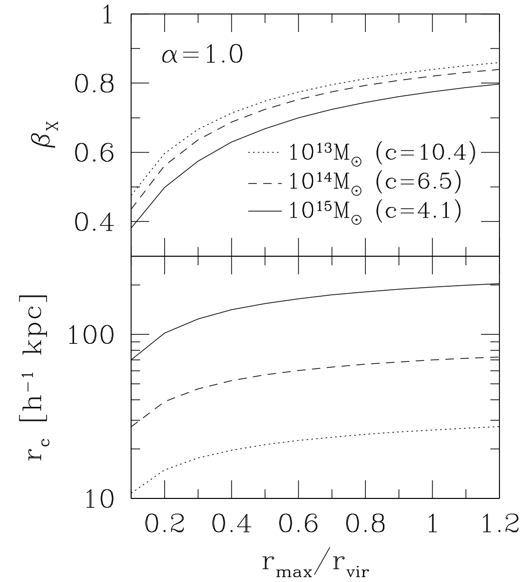

Figure 10. Sensitivity of parameters of the spherical β profile to the maximum radius, $r_{\rm max}$, that is used for fitting the X-ray surface brightness profile to the β profile. The maximum radius is in units of the virial radius. The top panel shows the outer slope $\beta_{\rm X}$, while the bottom panel shows the core radius $r_c^{\rm X}$. The solid lines, dashed lines, and dotted lines indicate the virial mass of 10^{15}, 10^{14}, and 10^{13} $M_{\odot}$, respectively. The corresponding concentration parameter, c, to the mass is quoted. The dark matter density profile for $\alpha = 1$ is used.

$$\propto \int_{-\infty}^{\infty} dl \left[y_{\rm gas}\left(\sqrt{x^2+l^2}\right)\right]^{(\gamma+3)/2}. \qquad (32)$$

Figure 9 shows the predicted X-ray surface brightness profiles together with the best-fitting spherical β profiles. The predicted X-ray surface brightness profile is quite similar to the β profile (Makino et al. 1998; Suto et al. 1998).

4.2 Examining observational selection effects

The main issue in comparing quantitatively the predicted X-ray profiles to the observed ones is out to which the radius the observed X-ray profile is typically fitted to the β profile. Our predicted profile has a slope continuously decreasing from 0 to -3 with radius, corresponding to $\beta_{\rm X}$ varying from 0 to 1; thus, the larger outermost radius one uses for the fit, the larger $\beta_{\rm X}$ one obtains. The top panel of figure 10 shows how sensitive $\beta_{\rm X}$ is to the maximum radius, $r_{\rm max}$, that is used for the fit. This effect was also observed from hydrodynamic simulations by Navarro et al. (1995). We find that the sensitivity of $\beta_{\rm X}$ to $r_{\rm max}$ is comparable to the mass dependence of $\beta_{\rm X}$. In other words, any correlation between $\beta_{\rm X}$ and mass can be created by changing $r_{\rm max}$ slightly but systematically. The bottom panel of the figure plots the sensitivity of the core radius to $r_{\rm max}$.

In order to make a meaningful comparison between our predicted X-ray profiles and observations we have to characterize the observational selection effect. In X-ray observations, $r_{\rm max}$ is the radius at which the background noise starts to dominate the X-ray surface brightness. Hence, we roughly estimate $r_{\rm max}$ by equating $I_{\rm X}(r_{\rm max})$ to the background noise level BG,

$$BG = I_{\rm X}(r_{\rm max}) \propto \rho_{\rm gas}^2(0) T_{\rm gas}^{1/2} \left(\frac{r_{\rm max}}{r_{\rm s}}\right)^{2s_*+1} r_{\rm s}, \qquad (33)$$

where $s_* \sim -3$ is a slope of the gas density profile given by equation (22) with $x_* = c$. As $c \propto T_{\rm gas}^{-3/10}$, $\rho_{\rm gas}(0) \propto c^3 \propto T_{\rm gas}^{-9/10}$, and $r_{\rm s} = r_{\rm vir}/c \propto T_{\rm gas}^{4/5}$. After some algebra, one obtains

$$\frac{r_{\rm max}}{r_{\rm vir}} \propto T_{\rm gas}^{3/10+1/(4s_*+2)} (BG)^{1/(2s_*+1)}. \qquad (34)$$

Thus, if BG is assumed not to vary significantly from observation to observation, $r_{\rm max}/r_{\rm vir} \propto T_{\rm gas}^{3/10+1/(4s_*+2)} \approx T_{\rm X}^{1/5}$.

Figure 11 plots $r_{\rm max}$ in units of r_{500} for a number of clusters and groups with the emission-weighted mean temperatures of $0.4 - 10$ keV. The data are taken from Mohr, Mathiesen & Evrard (1999) and Helsdon & Ponman (2000). r_{500} is calculated from the emission-weighted mean temperature through the normalization found by Mohr et al. (1999):

$$r_{500} = 2.37 \left(\frac{T_{\rm X}}{10~{\rm keV}}\right)^{1/2} \left(\frac{h}{0.5}\right)^{-1}~{\rm Mpc}. \qquad (35)$$

Despite the large scatter there is some evidence that $r_{\rm max}/r_{500}$ increases with $T_{\rm X}$. The figure also plots (solid line) an estimated scaling of the selection effect from equation (34) normalized so as to have $r_{\rm max} = 0.8 r_{500}$ at 6 keV, chosen to agree with the observational data. Equation (34) seems to capture a rough tendency of the actual selection effect, while the large scatter around the solid line in the

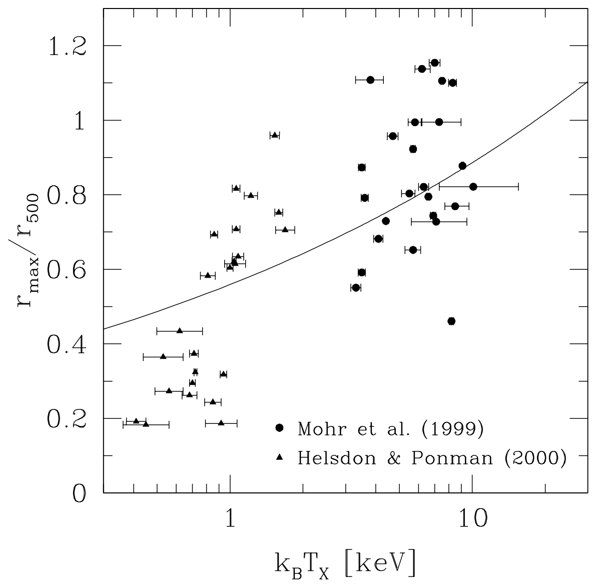

Figure 11. Observational maximum radii, $r_{\max}$, used for fitting the observed X-ray surface brightness profiles to the β profile, as a function of the emission-weighted mean temperature T_X. $r_{\max}$ is in units of r_{500}. The circles are the data taken from Mohr et al. (1999), while the triangles are from Helsdon & Ponman (2000). The solid line indicates an estimate of the temperature dependence of the selection effect caused by the background noise (equation (34)). Note that r_{500} is about one half of the virial radius (see figure 1).

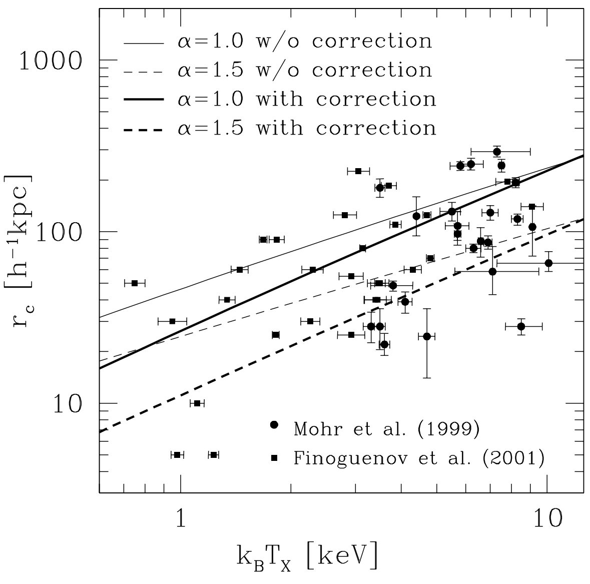

Figure 12. Predicted core radii r_c^X as a function of the emission-weighted mean temperature T_X in comparison to the observational data from Mohr et al. (1999) (circles) and Finoguenov et al. (2001) (squares). The solid lines represent $\alpha = 1$, while the dashed lines represent $\alpha = 3/2$. The thin lines are calculated by fitting the predicted X-ray surface brightness profiles to the β model out to r_{500}. The thick lines take into account the observational selection effect on the maximum radius used for the fitting (see figure 11 or equation (34)).

figure would be explained by the fact that the background level, BG, is varying substantially from observation to observation (or that clusters are not universal on the individual basis).

The selection effect is summarized as follows: *For the cooler haloes, the smaller $r_{\max}/r_{500}$ is used for fitting the observed X-ray surface brightness profiles to the β profile.* This leads one to have smaller β_X and core radii for the cooler haloes than those for the hotter haloes, according to our predicted X-ray surface brightness profile. We see below more quantitatively how the selection effect affects the comparison.

4.3 X-ray core radii

Figure 12 compares our predicted core radii to the observational data from Mohr et al. (1999) and Finoguenov et al. (2001). We have chosen the samples from Mohr et al. (1999) to which the double-β analysis is not applied. The predictions corrected for the selection effect due to the background noise (equation (34)) are plotted in the thick lines, while the thin lines show the ones without the correction. The latter ones are fitted out to r_{500} regardless of the temperature. The correction makes the core radii smaller than those without the correction, as the gas density profile is shallower in the inner region than in the outer region. We find that the predicted core radii from our polytropic gas model are in good agreement with the observational data. The predicted core radii for $\alpha = 3/2$ are systematically smaller than those for $\alpha = 1$. Qualitatively this is what one would expect, as the former profiles are more centrally concentrated than the latter ones at small radii (the rescaling of concentration with 1.7 only brings the outer profile in agreement, while in the centre differences remain). This is easily seen in figure 9 in which the predicted X-ray profiles are shown. However, both models are acceptable given the large scatter in the data. We have also tried other concentration parameters and find that these affect the core radii less than the change of the inner slope. Inner gas profiles are therefore a potentially powerful probe of dark matter distribution at small distances. However, for a proper description of this region our polytropic assumption is no longer valid and one must generalize it to account for the observed decrease in the temperature towards the centre (McNamara et al. 2000; Allen et al. 2001a, 2001b; Arnaud et al. 2001a, 2001b; Kaastra et al. 2001). We plan to investigate this in the future.

Figure 12 shows the dependence of the core radii on temperature. The positive correlation seen in the figure can be explained mostly by the fact that hotter haloes are larger. In order to investigate the concentration dependence on mass or temperature we plot in figure 13 r_{500}/r_c^X as a function of the emission-weighted mean temperature. Our predictions for $\alpha = 1$ are in good agreement with the data. There is a marginal tendency for cooler haloes to have a higher r_{500}/r_c^X, and hence a higher concentration. The concentration parameter is also plotted in the thin lines.

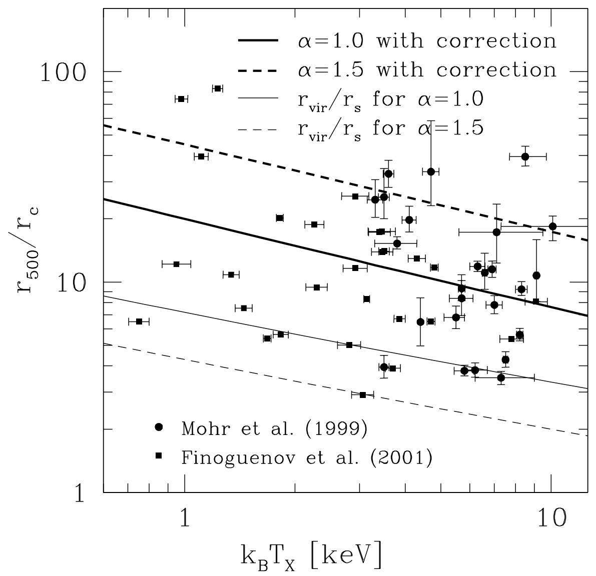

Figure 13. Predicted ratio of overdensity radii, r_{500}, to core radii, $r_{\rm c}^{\rm X}$, as a function of the emission-weighted mean temperature $T_{\rm X}$ in comparison to the observational data from Mohr et al. (1999) (circles) and Finoguenov et al. (2001) (squares). The solid lines represent $\alpha = 1$, while the dashed lines represent $\alpha = 3/2$. The thick lines plot $r_{500}/r_{\rm c}^{\rm X}$ with taking into account the observational selection effect on the maximum radius used for the fitting (see figure 11 or equation (34)). The thin solid lines show the concentration parameter $c \equiv r_{\rm vir}/r_{\rm s}$.

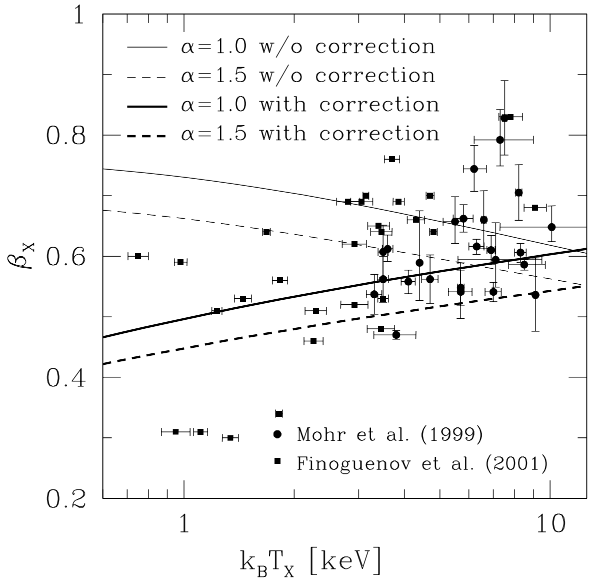

Figure 14. Predicted outer slope, $\beta_{\rm X}$, as a function of the emission-weighted mean temperature $T_{\rm X}$ in comparison to the observational data from Mohr et al. (1999) (circles) and Finoguenov et al. (2001). The solid lines represent $\alpha = 1$, while the dashed lines represent $\alpha = 3/2$. The thin lines are the relations obtained by fitting the predicted X-ray surface brightness profile to the β model out to r_{500}. The thick lines take into account the observational selection effect on the maximum radius used for the fitting (see figure 11 or equation (34)).

It shows the same correlation as $r_{500}/r_{\rm c}^{\rm X}$, supporting this interpretation. We find $r_{500}/r_{\rm c}^{\rm X} \sim 0.4c$ for $\alpha = 1$, and $r_{500}/r_{\rm c}^{\rm X} \sim 0.1c$ for $\alpha = 1.5$. The former gives $r_{\rm c}^{\rm X} \sim 0.2 r_{\rm s}$, while the latter gives $r_{\rm c}^{\rm X} \sim 0.05 r_{\rm s}$. The former is similar to Makino et al. (1998) despite the fact that our model does not assume the isothermality. Note that their predicted core radii are systematically smaller than observational data, because the concentration parameter they use is larger on cluster mass scales than what we use.

An important observation from figure 12 is that the data show fairly large scatter in $r_{500}/r_{\rm c}^{\rm X}$ ratio. While this could be explained to some extent by the uncertainties in the observational selection effect, it could also imply that the universal gas profile as proposed in this paper can only be valid in a statistical sense, and thus individual clusters may deviate from it significantly. This is consistent with the findings from numerical simulations (Thomas et al. 2001), but has not been previously shown with the observational data on cluster mass scales.

4.4 X-ray outer slope $\beta_{\rm X}$

Figure 14 plots the outer slope, $\beta_{\rm X}$, as a function of the emission-weighted mean temperature $T_{\rm X}$. The observational data show a positive correlation between $\beta_{\rm X}$ and $T_{\rm X}$, which is consistent with what Horner, Mushotzky & Scharf (1999) and Lloyd-Davies, Ponman & Cannon (2000) found in a different observational catalogue. Similarly, Neumann & Arnaud (1999) pointed out a positive correlation between $\beta_{\rm X}$ and core radii. Given the observational evidence that the core radius increases with the emission-weighted mean temperature, it implies that $\beta_{\rm X}$ should also increase with the temperature.

Our model predicts a *negative* correlation between the core radii and slopes if the X-ray profile is fitted to the β profile out to the *fixed* overdensity radius, for example, r_{500}. This is easy to understand: the smaller the mass is, the more centrally concentrated the profile becomes and the larger $\beta_{\rm X}$ and core radius one obtains. However, we must also include the surface brightness cutoff selection effect discussed above. Once we correct for it the predicted $\beta_{\rm X}$ comes to very good agreement with the data. This is explicitly shown in figure 14. The selection effect makes the maximum radii used for the fit smaller for cooler haloes. As we have shown, this effect makes $\beta_{\rm X}$ smaller (see figure 10). It would be particularly prominent for group sample of Helsdon & Ponman (2000), where $r_{\rm max}$ is very small compared to r_{500}. This is in fact seen in the data and the obtained values for this sample are $\beta_X \sim 0.3$ (Helsdon & Ponman 2000). Thus, we conclude that the positive correlation between $\beta_{\rm X}$ and $T_{\rm X}$ could be caused by the observational selection effect and the trend would be opposite if X-ray profiles were fitted to the β profile out to a fixed overdensity radius.

5 SURFACE BRIGHTNESS PROFILES OF THE SUNYAEV–ZEL'DOVICH EFFECT

The Sunyaev–Zel'dovich (SZ) effect (Zel'dovich & Sunyaev 1969) is now established as a very powerful observational tool for imaging clusters (e.g., Carlstrom et al. 2000). Measurement of surface brightness profiles of the SZ effect gives a projected gas pressure density of clusters. In order to extract the gas density profile from the measurement, we need to deproject the measured surface brightness profile. Thus, we need to have an appropriate model to parameterize the profile. As often done in X-ray observations, the surface brightness profile of the SZ effect has also been parametrized in terms of the β profile:

$$I_{\rm SZ}(r) = I_{\rm SZ}(0)\left[1+\left(\frac{r}{r_{\rm c}^{\rm SZ}}\right)^2\right]^{1/2-3\beta_{\rm SZ}/2}. \quad (36)$$

We compare our predicted profiles of the SZ effect to the β profile. The SZ profile is calculated as

$$I_{\rm SZ}(x) \propto \int_{-\infty}^{\infty} dl\ P_{\rm gas} \propto \int_{-\infty}^{\infty} dl \left[y_{\rm gas}\left(\sqrt{x^2+l^2}\right)\right]^{\gamma}. \quad (37)$$

Figure 15 shows the predicted SZ surface brightness profiles together with the best-fitting β profiles. The fit is performed out to either the virial radius (dashed lines), or r_{500} (dotted lines) at which the dark matter density is 500 times the critical density of the universe. The SZ profiles are substantially shallower than the X-ray profiles, as found out by comparing this figure to figure 9. This comes from the different weights in the gas density for the SZ and X-ray profiles. The SZ surface brightness is weighted by $\rho_{\rm gas}$, while the X-ray surface brightness is weighted by $\rho_{\rm gas}^2$. Although the β profile gives a reasonable fit to our profile, the slope of the fitted profile is quite sensitive to the outermost radius used for the fit. This tendency is also seen in fitting the X-ray surface brightness profiles to the β profile, indicating that neither the X-ray nor the SZ surface brightness profiles are properly described by a simple power-law shape such as the β profile.

If the gas is isothermal, then the β profile implies that the gas density profile is given by

$$\rho_{\rm gas}(r) = \rho_{\rm gas}(0)\left[1+\left(\frac{r}{r_{\rm c}}\right)^2\right]^{-3\beta/2}, \quad (38)$$

with $r_{\rm c} = r_{\rm c}^{\rm X} = r_{\rm c}^{\rm SZ}$ and $\beta = \beta_{\rm X} = \beta_{\rm SZ}$. As we have shown, our predicted profiles appreciably deviate from this spherical isothermal β model. One way to quantify *how much* the β model deviates from our model is to calculate $\beta_{\rm SZ}/\beta_{\rm X}$ and $r_{\rm c}^{\rm SZ}/r_{\rm c}^{\rm X}$. If the spherical isothermal β model predicts exactly the same surface brightness profiles as our model, then those ratios should be 1. Figure 16 shows predicted $\beta_{\rm SZ}/\beta_{\rm X}$ in the top panel and $r_{\rm c}^{\rm SZ}/r_{\rm c}^{\rm X}$ in the bottom panel. They are plotted as a function of the maximum radius, $r_{\rm max}$, which is the outermost radius used for the fit. We find that $\beta_{\rm SZ}/\beta_{\rm X} = 1.15 - 1.2$ and $r_{\rm c}^{\rm SZ}/r_{\rm c}^{\rm X} = 1.1 - 1.15$ for a relevant range of $r_{\rm max}$. Thus, we predict that the SZ surface brightness profiles give systematically larger fitted parameters than the X-ray profiles (by roughly 20%). This prediction can be tested by upcoming observations.

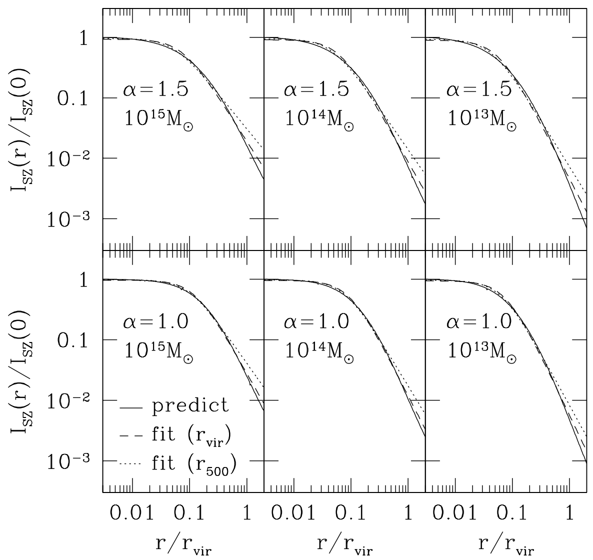

Figure 15. Predicted surface brightness profiles of the Sunyaev–Zel'dovich effect (solid lines) and the best-fitting spherical β profiles (dashed and dotted lines). The fit is performed out to either the virial radius (dashed lines) or r_{500} (dotted lines). Note that r_{500} is about one half of the virial radius (see figure 1). The top panels use the dark matter density profile for $\alpha = 3/2$, while the bottom panels use the one for $\alpha = 1$. From left to right panels, each panel shows the case of $M = 10^{15}$, 10^{14}, and 10^{13} $M_\odot$, respectively.

6 MASS–TEMPERATURE RELATION

Masses and emission-weighted mean temperatures of many observed clusters and groups are known to be very tightly correlated. This correlation is called the mass–temperature scaling relation. Qualitatively it arises as a consequence of the virial relation between the virial mass and the virial temperature, $T_{\rm gas}(r_{\rm vir}) \propto M_{\rm vir}^{2/3}$. Traditionally workers have used a self-similar model with a constant concentration to explain this relation, which gives rise to the same scaling as for the virial quantities. The normalization of the relation has been obtained from numerical simulations. In our model, the scaling relation is described by equation (20). For comparison with observations, we will use the emission-weighted mean temperature. Hence, we must use the mean emission-weighted normalization factor, $\eta_{\rm X}$ (equation (29)), when relating the mass to the temperature. Similarly we will use M_{500} instead of $M_{\rm vir}$. Since the concentration in our model depends on the mass, the resulting mass–temperature relation is no longer given by the self-similar relation such as $T_{\rm X} \propto M_{500}^{2/3}$. Moreover, the overall normalization is no longer a free parameter but fixed in our model for a given universal dark matter density profile. We will show below that both features bring the model predictions into better agreement with the data than the self-similar model.

We first begin by discussing the mass–temperature relation for hotter clusters than 3 keV. The X-ray observations suggest that the observed emission-weighted mean normalization is slightly, but systematically, higher than that is

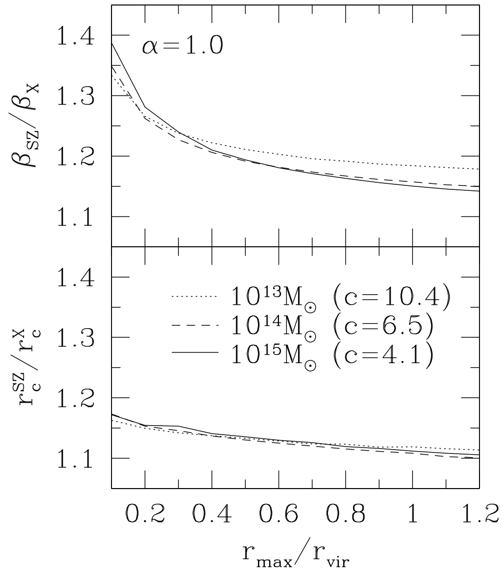

Figure 16. Comparison of fitted parameters of the β profile obtained from X-ray and the Sunyaev–Zel'dovich surface brightness profiles. The ratio of the SZ outer slope to the X-ray outer slope, β_{SZ}/β_X, is plotted in the top panel, while the one of the SZ core radius to the X-ray core radius, r_c^{SZ}/r_c^X, is plotted in the bottom panel. They are shown as a function of the maximum radius, r_{max}, out to which the surface brightness profiles are fitted to the β profile. The maximum radius is in units of the virial radius. The solid lines, dashed lines, and dotted lines indicate the virial mass of 10^{15}, 10^{14}, and 10^{13} $M_\odot$, respectively. The corresponding concentration parameter, c, to the mass is quoted. The dark matter density profile for $\alpha = 1$ is used.

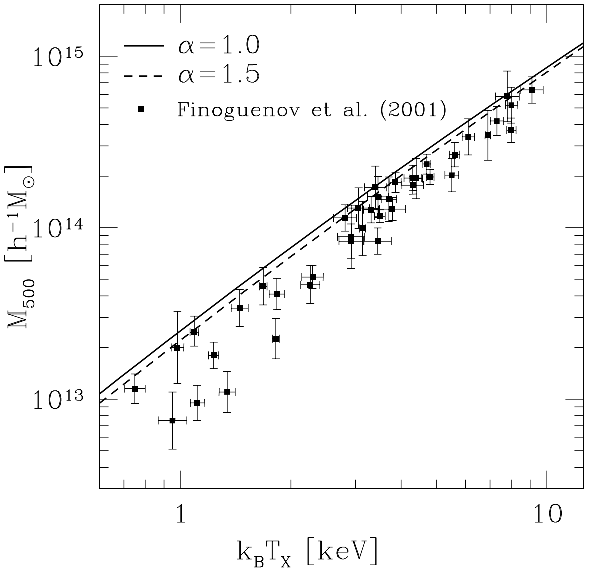

Figure 17. Predicted mass–temperature scaling relations at $z = 0$ (solid and dashed lines) compared with the observational data from Finoguenov et al. (2001) (squares). The solid line represents $\alpha = 1$, while the dashed line represents $\alpha = 3/2$.

predicted by hydrodynamic simulations (Horner et al. 1999; Nevalainen, Markevitch, & Forman 2000; Finoguenov et al. 2001). It means a higher emission-weighted mean temperature for a given mass. For instance, Finoguenov et al. (2001) found that their sample above 3 keV gives about 50% higher normalization, $\eta_X(\mathrm{obs}) \sim 2.0$, than the simulation by Evrard et al. (1996), which give $\eta_X(\mathrm{sim}) \sim 1.3$. However, as noted previously, there is scatter among different hydrodynamic simulations: Bryan & Norman (1998) give $\eta_X(\mathrm{sim}) = (3/2) f_T \sim 1.2$, Eke et al. (1998) give $\eta_X(\mathrm{sim}) = (3/2)\overline{\beta}_{TM}^{-1} \sim 1.5$, Yoshikawa et al. (2000) give $\eta_X(\mathrm{sim}) = \gamma \sim 1.6$ and Thomas et al. (2001) give $\eta_X(\mathrm{sim}) \sim 1.5$. Here, the second equality quotes the author's notation for simplicity in comparison. Presumably this scatter is caused by varying resolution, numerical techniques, methods of analyzing the simulations, and so on, in the simulations.

Our model predicts a normalization at the upper end of the simulations, $\eta_X \gtrsim 1.5 - 1.8$, depending on α and the mass of haloes (see figure 6). This means that it fits the observational data reasonably well in the high temperature regime. Figure 17 compares our predictions for the mass–temperature relation at $z = 0$ (solid and dashed lines) to the local observational data from Finoguenov et al. (2001). The agreement between the model and the data is reasonably good, especially for $k_BT_X > 3$ keV, where our model is only 20% above the observations. Such small discrepancies could easily be explained by either systematic effects in observations or by the scatter in the cluster properties, which may increase the average polytropic index slightly (we find excellent agreement for $\gamma = 1.2$). Note that additional kinetic energy term in the hydrostatic equilibrium, which is expected to be at 10-20% level (Navarro et al. 1995), does not bring our model into better agreement, since the masses in both the data and the model are underestimated by the same amount.

Finoguenov et al. (2001) excised central regions of the clusters when they measured the emission-weighted temperatures. Unfortunately, it is not clear what the inner cut-off radius is used in their analysis. Hence, we compared the emission-weighted temperatures calculated excluding the region inside $r_{cut} = 0.01c$, $0.05c$, and $0.1c$ to the one without the excision. $0.1c$ corresponds to 340 and 150 kpc for $M_{500} = 10^{15}$ and 10^{14} $M_\odot$, respectively, so it is a fairly extreme excision. In reality, the excised region is likely to be smaller than the core radius that is about $30 - 300$ kpc (see figure 12). Thus, $r_{cut} = 0.1c$ gives a conservative upper limit on the effect. We find that $r_{cut} = 0.1c$ reduces the emission-weighted temperature by about 5% and 10% for $M_{500} = 10^{15}$ $M_\odot$ and 10^{14} $M_\odot$, respectively. The smaller haloes are more affected by the excision, as they are more centrally concentrated. The excision also eliminates the difference between $\alpha = 1$ and 1.5 models. The cut-off radius of below $0.05c$ has negligible effect on the emission-weighted temperature compared to the no excision case. Figure 17 plots the predictions without the excision.

The X-ray observations of cooler (< 3 keV) clusters or groups suggest that the slope of the mass–temperature scaling relation deviates from the virial scaling relation,

$T_{\mathrm{X}} \propto M_{500}^{2/3}$ (Nevalainen et al. 2000; Sato et al. 2000; Finoguenov et al. 2001). It becomes steeper towards the cooler haloes, which indicates they have a higher emission-weighted mean temperature than what is predicted by the virial scaling relation. This is exactly what one would predict from the model where the concentration decreases with the mass.

Figure 6 shows how our predicted emission-weighted mass–temperature normalization factor depends on the virial mass. The trend is in the desired direction: less massive haloes have higher normalizations and thus higher temperatures than predicted by the virial scaling relation. This is due to the fact that less massive haloes are more centrally concentrated than more massive ones.

Figure 17 shows that our predictions for cooler haloes fit the observational data better, in contrast to the predictions of the hydrodynamic simulations where the dependence of the normalization factor on the halo mass has not been observed (or studied). This could be explained simply by the lack of resolution in the simulations for the smaller haloes. This would not be surprising given how sensitive the emission weighted mean temperature is to the central concentration of the cluster, but must be verified with better simulations. The predictions for higher α or concentrations fit the data even better, although in all cases the predictions are, on average, still above the data. Within our model this could be explained by a steeper concentration dependence on mass, while the alternative suggestion that the temperature has been raised by some energy (or entropy before the infall) injection is also possible (Bialek, Evrard & Mohr 2000). These results suggest that the emission-weighted mean temperature is very sensitive to the central region of the haloes and that a simple self-similar model cannot be used to compare the observations to the models. A more realistic model beyond the self-similar model that includes the concentration parameter as a function of the mass removes much of the discrepancy with the data.

7 DISCUSSION AND CONCLUSIONS

In this paper, we have constructed a model for predicting gas density and temperature profiles that are analogous to the universal dark matter density profile developed for dark matter. We assume that the gas density traces the dark matter density in the outer parts of haloes, which seems to be verified in a number of hydrodynamic simulations. This assumption, together with the hydrostatic equilibrium and spherical symmetry, uniquely specifies the gas density and temperature profiles that are related through a polytropic equation of state. The polytropic assumption breaks down in the inner parts of the cluster (well inside the gas core) as shown by recent *Chandra* (McNamara et al. 2000; Allen et al. 2001a, 2001b) and *XMM–Newton* (Arnaud et al. 2001a, 2001b; Kaastra et al. 2001) temperature profiles, but for the outer parts seems to be in good agreement with both simulations and observations. Our predicted gas density and gas temperature profiles agree with the hydrodynamic simulations both in the profiles and in the overall amplitude. The predicted slope of the polytropic index is $\gamma \simeq 1.15$, which is in remarkable agreement with the observational data from Finoguenov et al. (2001).

We have made predictions for the core radii and the outer slopes, β, that are parameters empirically characterizing surface brightness profiles of X-ray and the Sunyaev–Zel'dovich (SZ) effect. Fitting the predicted X-ray profiles to those parameters, we found that our predicted X-ray core radii and X-ray outer slopes, β_{X}, are in good agreement with the observations, after the correction for the observational surface brightness selection effect. This makes β_{X} increase with the temperature, explaining the observed trend. The X-ray core radius is less sensitive to this selection effect and is predicted to increase with the temperature, in agreement with the observations.

We calculated the SZ surface brightness profiles and fitted them to the β profile. The fitted results are very sensitive to the outermost radius used for the fit, suggesting that the β profile is not a proper description of the profile. The core radii and β fitted from the SZ profiles are predicted to be systematically larger than those fitted from the X-ray profiles if the same $r_{\max}$ is used. In addition, for the SZ one would expect to use the larger $r_{\max}$ in the fit, further increasing β_{SZ}.

We have predicted the mass–temperature scaling relation, and compared it to the observational data as well as hydrodynamic simulations. We found good agreement between our predictions and the observations, especially for hotter clusters. For cooler clusters and groups, we found better agreement than the hydrodynamic simulations that tend to have lower temperatures than the observations. The disagreement between our predictions and the simulations could be caused by the limited resolution in the simulations, as the emission-weighted mean temperature is quite sensitive to the gas distribution in the centre. On the other hand, it is also possible that some physics is still missing in the simulations, but that does not show up in our phenomenological description of the temperature–density relation. Careful studies of the numerical resolution and additional physics are needed to resolve this issue (Suginohara & Ostriker 1998; Pearce et al. 2000; Lewis et al. 2000; Yoshikawa et al. 2000; Muanwong et al. 2001). Some disagreement between our model and the observational data remains for the mass concentration dependence obtained from pure N-body simulations, but this is removed if a steeper dependence is invoked. The baryonic cooling contraction and subsequent readjustment of the dark matter generically increases concentration and the effect should be more important for smaller masses where a larger fraction of the gas is transformed into stars. This trend is in the right direction and also agrees with the results of Sato et al. (2000). We plan to investigate this in more detail in the future.

We have not attempted to predict other scaling relations, such as the X-ray luminosity–temperature relation and the central entropy–temperature relation. In order to predict them we need at least one additional uncertain parameter, the gas mass fraction, which is a ratio of the gas mass to the dark matter mass. This parameter is not constrained by our method, as it does not appear in the hydrostatic equilibrium equation. While the baryon mass fraction is believed to be equal to the cosmic mean baryon fraction $\Omega_{\mathrm{b}}/\Omega_{\mathrm{m}}$ on large scales (White et al. 1993), observational evidence suggests that the gas mass fraction increases with mass (Arnaud & Evrard 1999; Mohr et al. 1999). This could be explained if some non-negligible fraction of the gas was transformed into stars or expelled out of the halo. Since the X-ray luminosity is in proportion to the gas mass fraction squared and the central entropy is in proportion to the gas mass fraction to $-2/3$ power, the resultant predictions are significantly affected by the uncertainty in the gas mass fraction. The luminosity–temperature relation and the central entropy–temperature relation can be explained without invoking any preheating models if one allows the gas mass fraction to vary with the temperature (Bryan 2000). Therefore, even without changing our model we should be able to predict those relations consistent with observations with an appropriate gas mass fraction mass dependence. In addition, gas luminosity is strongly affected by the size and density of the core region and even small modifications in the profile can lead to large changes in luminosity, which is thus not robustly predicted with our model.

E. K. acknowledges financial support from the Japan Society for the Promotion of Sciences. U. S. acknowledges the support of NASA and Packard and Sloan Foundation Fellowships.

REFERENCES

Allen S. W., Ettori S., Fabian A. C., 2001a, MNRAS, in press (astro-ph/0008517)
Allen S. W. et al., 2001b, MNRAS, in press (astro-ph/0101162)
Arnaud M., Evrard A. E., 1999, MNRAS, 305, 631
Arnaud M. et al., 2001, A&A, 365, L67
Arnaud M., Neumann D. M., Aghanim N., Gastaud R., Majerowicz S., Hughes J. P., 2001, A&A, 365, L80
Bialek J. J., Evrard A. E., Mohr J. J., ApJ, submitted (astro-ph/0010584)
Binney J., Tremaine S., 1987, Galactic Dynamics, Princeton Univ. Press, Princeton, NJ
Bryan G. L., 2000, ApJ, 544, L1
Bryan G. L., Norman M. L., 1998, ApJ, 495, 80
Bullock J. S., Kolatt T. S., Sigad Y., Somerville R. S., Kravtsov A. V., Klypin A. A., Primack J. R., Dekel A., 2001, MNRAS, 321, 559
Carlstrom J. E., Joy M. K., Grego L., Holder G. P., Holzapfel W. L., Mohr J. J., Patel S., Reese E. D., 2000, Physica Scripta Volume T, 85, 148
Eke V. R., Navarro J. F., Frenk C. S., 1998, ApJ, 503, 569
Eke V. R., Navarro J. F., Steinmetz, 2000, ApJ, submitted (astro-ph/0012337)
Evrard A. E., Metzler C. A., Navarro J. F., 1996, ApJ, 469, 494
Finoguenov A., Reiprich T. H., Böhringer H., 2001, A&A, 368, 749
Frenk C. S. et al., 1999, ApJ, 525, 554
Helsdon S. P., Ponman T. J., MNRAS, 315, 356
Horner D. J., Mushotzky R. F., Scharf C. A., 1999, ApJ, 520, 78
Jing Y. P., Suto Y., 2000, ApJ, 529, L69
Kaastra J. S., Ferrigno C., Tamura T., Paerels F. B. S., Peterson J. R., Mittaz J. P. D., 2001, A&A, 365, L99
Klypin A., Kravtsov A. V., Bullock J., Primack J., 2001, ApJ, in press (astro-ph/0006343)
Lacey C., Cole S., 1993, MNRAS, 262, 627
Lewis G. F., Babul A., Katz N., Quinn T., Hernquist L., Weinberg D. H., 2000, ApJ, 536, 623
Lloyd-Davies E. J., Ponman T. J., Cannon D. B., MNRAS, 315, 689
Makino N., Sasaki S., Suto Y., 1998, ApJ, 497, 555
McNamara B. R. et al., 2000, ApJ, 534, L135
Mohr J. J., Mathiesen B., Evrard A. E., 1999, ApJ, 517, 627
Moore B., Governato F., Quinn T., Stadel J., Lake G., 1998, ApJ, 499, L5
Muanwong O., Thomas P. A., Kay S. T., Pearce F. R., Couchman H. M. P., 2001, ApJ, 552, L27
Nakamura T. T., Suto Y., 1997, Prog. Theor. Phys., 97, 49
Navarro J. F., Frenk C. S., White S. D. M., 1995, MNRAS, 275, 720
Navarro J. F., Frenk C. S., White S. D. M., 1996, ApJ, 462, 563
Navarro J. F., Frenk C. S., White S. D. M., 1997, ApJ, 490, 493
Neumann D. M., Arnaud M., 1999, A&A, 348, 711
Netterfield B. et al., 2001, ApJ, submitted (astro-ph/0104460)
Nevalainen J., Markevitch M., Forman W., 2000, ApJ, 532, 694
Peebles P. J. E., 1980, The Large Scale Structure of the Universe, Princeton Univ. Press, Princeton, NJ
Pearce F. R., Thomas P. A., Couchman H. M. P., Edge A. C., MNRAS, 317, 1029
Sato S., Akimoto F., Furuzawa A., Tawara Y., Watanabe M., 2000, ApJ, 537, L73
Seljak U, 2000, MNRAS, 318, 203
Suginohara T., Ostriker J. P., 1998, ApJ, 507, 16
Suto Y., Sasaki S., Makino N., 1998, ApJ, 509, 544
Thomas P. A., Muanwong O., Pearce F. R., Couchman H. M. P., Edge A. C., Jenkins A., Onuora L., 2001, MNRAS, 324, 450
White S. D. M., Navarro J. F., Evrard A. E., Frenk C. S., 1993, Nat, 366, 429
Yoshikawa K., Jing Y. P., Suto Y., 2000, ApJ, 535, 593
Zel'dovich Ya. B., Sunyaev R. A., 1969, Ap&SS, 4, 301